Nano World Journal

https://doi.org/10.17756/nwj.2024-s2-003

Research Article

Open Access

Impact of Solution Treatment on the Microstructure, Ultimate Tensile Strength and Weld Nugget Hardness Characteristics of Friction Stir Welded Joints of AA6082 Hybrid Composites

Umar Mohamed Jamaludeen*

Department of Mechanical Engineering, Annamalai Polytechnic College, Chettinad, Tamil Nadu, India

***Correspondence to:**
Umar Mohamed Jamaludeen
Department of Mechanical Engineering,
Annamalai Polytechnic College,
Chettinad, Tamil Nadu, India.
E-mail: umarmjamaludeen@gmail.com

Received: August 19, 2024
Accepted: November 20, 2024
Published: November 25, 2024

Citation: Jamaludeen UM. 2024. Impact of Solution Treatment on the Microstructure, Ultimate Tensile Strength and Weld Nugget Hardness Characteristics of Friction Stir Welded Joints of AA6082 Hybrid Composites. *NanoWorld J* 10(S2): S22-S31.

Published by United Scientific Group

Abstract

This research emphases the impact of solution annealing (post-weld heat treatment(PWHT)) on the ultimate tensile strength (UTS) and weld nugget hardness (WNH) characteristics of friction stir welded (FSW) joints of AA6082/3 wt.% ZrO_2/5 wt.% B_4C aluminium matrix hybrid composites (AMMHCs). The FSW joints underwent solution annealing followed by numerous ageing treatments. Solution annealing is conducted at 450 °C in the AMMHCs, which are FSW with the low (28.55 kJ/mm), high (114.23 kJ/mm) heat input (HHI) conditions, and optimum FSW process parameters (57.83 kJ/mm) HI (OHI) conditions. The soaking period is conducted for 60 minutes and subsequently quenching by water and artificial ageing conducted at 120 °C for a soaking duration of 1 day. Solution annealing significantly influences grain growth, phase transformation, and the alteration of microstructures within various regions of the weldment, including the welded nugget zone (WNZ), thermo-mechanically affected zone (TMAZ), heat-affected zone (HAZ), and base metal (BM). Furthermore, understanding these microstructural changes aids in enhancing mechanical properties such as UTS and WNH. The UTS and WNH seemed to be increased at 450 °C. The FSW joints attained with FSW process parameters HI conditions produced the fine grains and maximum UTS of 248 MPa and microhardness of 118 HV after solution annealing at 450 °C.

Keywords

Solution annealing, Microstructure, Friction stir welding

Introduction

AA6082 alloy is being unique aluminium alloy and considered as high as UTS alloy with excellent corrosion resistance in the series of aluminium 6000. When AA6082 alloys are fabricated as aluminium metal matrix hybrid composites, it exhibits better resistance to wear, high strength and low thermal coefficient of expansion compared to AA6082 alloy. AA6082 hybrid composites replaces AA6061 in many applications like trusses, bridges, cranes, ore ships, beer barrels and milk churns [1]. The fabrication of intricate equipment/components of AMMHCs depends on effective joining methods such as solid state and fusion welding processes, that are still rely on specific material and process. These AMMHCs are non-weldable using fusion welding techniques due to the (a) occurrence of segregation and undesirable reactions between the reinforcement particles and liquid aluminum in the fusion zone, (b) improper mixing of parent and filler materials [2, 3]. These issues can be overcome by adopting the FSW for these composites.

FSW is a sustainable solid-state welding technique, typically performed at temperatures ranging from 0.6 to 0.9 times the material's melting point to achieve uniform plasticization. The process employs a non-consumable tool comprising a shoulder and pin, traversing along the interface of abutting plates clamped onto a backing plate. Through the application of pressure and controlled travel and advancement speeds, friction between the tool shoulder and the plates generates the necessary heat for material plastic flow. FSW is renowned for enhancing the mechanical properties of joints in aluminum alloys (2XXX, 6XXX, and 7XXX series) and aluminum metal matrix composites. Despite its myriad benefits such as excellent dimensional stability, ease of weldability in the solid state, and reduced weld defects, FSW does have drawbacks, notably the tendency for softened welded joints, leading to diminished mechanical strength.

FSW induces residual stresses in the material due to the rapid heating and cooling cycles. PWHT helps in relieving these residual stresses, which can otherwise act as sites for crack initiation and propagation, thereby reducing the material's strength. Stress relief during PWHT contributes to improved mechanical properties. Furthermore, the FSW zone experiences elevated temperatures due to mechanical stirring, altering the distribution of precipitates in the parent metal, thereby impacting the UTS and ductility of the welded joints. To address and improve these mechanical properties, PWHT is commonly employed on aluminum alloys and their composites.

Recent research efforts have been dedicated to unraveling the effects of PWHT on the mechanical properties of aluminum alloys and their composites. Gupta et al. [4] delved into the precipitation and hardening mechanisms within an Al-0.4%, Mg-1.3%, Si-0.25%, Fe alloy, pinpointing the hardness augmentation during natural aging to the precipitation of clusters and zones, with peak hardness attributed to β" particle precipitation. Similarly, Wang et al. [5] provided a thorough quantitative analysis of precipitation hardening in AA6111, revealing the coexistence of β" and Q' phases during aging, with the relative abundance of Q' increasing with prolonged aging at 180 °C.

Bahman et al. [6] explored the UTS of AA6061 alloys under various precipitation hardening and cold working conditions, noting an increase in UTS and decrease in ductility for samples subjected to specific aging treatments. Ahmad et al. [7] examined the impact of PWHT on the metallurgical and UTS properties of FSW aluminium alloy 6061 joints, highlighting a 4.7% UTS improvement with extended solution heat treatment. Jitlada et al. [8] discussed PWHT effects on the UTS, microhardness, toughness, and fracture surfaces of FSW AA6061-T651, finding a direct correlation between UTS and vickers hardness, while identifying lowest toughness at 6.2 J in PWHT specimens. Yousefpour et al. [9] analyzed PWHT's influence on the mechanical properties of FSW AA6061-T6 plates, revealing optimized Al_2O_3 nanoparticle distribution at specific welding speeds (WS).

Hossein et al. [10] explored precipitation hardening's effects in FSW of AA6061-T6 to AA2024-T6 plates, observing microstructural changes and increased joint efficiency post-treatment. Amir et al. [11] investigated T6 PWHT's impact on FSW AA8061, noting a reduction in the Portevin-Chatelier effect and enhanced mechanical properties through improved precipitation hardening. Bakkiyaraj et al. [12] examined PWHT's enhancement on FSW dissimilar AA6061 and AA7075-T6 joints, highlighting superior UTS and hardness with specific treatment regimes. Additionally, Monoj et al. [13] summarized processing stages and precipitation strengthening mechanisms of 6xxx aluminum series alloys, emphasizing the significance of proper homogenization for enhanced mechanical properties.

Srikanth et al. [14] explored traditional and cyclic heat treatments' effects on FSW dissimilar aluminum alloys AA5052 and AA6061, noting significant improvements in microhardness, UTS, and ductility with the newly-devised cyclic treatment. These studies collectively underscore PWHT's potential to alter microstructures and enhance the tensile strength and hardness of FSW joints, revealing a gap in research pertaining to PWHT on FSW AA6082 hybrid composites. Thus, this study aims to investigate PWHT's impact on the metallurgical, UTS, and hardness of FSW AA6082 hybrid composites under selected conditions: (a) low HI (LHI), (b) HHI, and (c) OHI.

Experimental Work

Material and FSWconditions

FSW is applied to AA6082 hybrid composite stir cast plates, each measuring 100 mm x 50 mm x 6 mm. The joining plates were longitudinally butt-joined parallel to the rolling direction using a FSW Machine. These plates are securely clamped onto the FSW machine table to attain a square butt configuration. The FSW tool, crafted from high carbon high chromium steel or D_2 tool steel (65 HRC), features a square pin profile measuring 4 mm in size and 5.7 mm in length, with an 18 mm shoulder diameter extending 15 mm in length. Rigidly fixed onto the rotational spindle, the tool is rotated clockwise and driven vertically downward and longitudinally during FSW to penetrate and weld the plates, regulated by a control panel. Axial load (AL) is applied to the plates via a hydraulic system. This study focuses on OHI, namely tool rotational speed (TRS), WS, and AL. Experimental results detailed in table 1 demonstrated that the highest UTS and work-hardening index (WNH) reach 239.28 MPa and 94.2 HV, respectively, at optimal welding conditions: TRS of 1030.95 rpm, WS of 38.50 mm/min, and AL of 5.88 kN, as determined through a desirability approach utilizing response surface methodology (RSM) and design expert software.

HI Calculation During FS Welding

Average heat input (AHI) calculation

The FSW tool's stirring motion induces significant plastic deformation and generates high temperatures within the weld nugget zone of FSW joints. Consequently, microstructural alterations occur in the welded zone of the advanced metal matrix hybrid composites (AMMHCs). The overall torque generated during this process is mathematically represented by equations 1 and 2 [15], while the AHI is quantified by equation 3 [16].

Table 1: Experimental results of optimum UTS and optimum WNH of AA6082 hybrid composites.

TRS (rpm)	WS (mm/min)	AL (kN)	UTS (MPa)	WNH (HV)
1030.95	38.50	5.88	239.28	94.2

$$T = T_s + T \quad (1)$$

$$T = 2 \text{ x } \mu \text{ x } F \text{ x } ((r_o / 3) + ((r_i^2 / (r_o{}^2) \text{ x } h)) \quad (2)$$

$$Q_{in} = \eta \text{ x } 2\pi NT/f \quad (3)$$

where, $T_{s\,=}$ Torque produced by the tool shoulder (nm), T_p = Torque produced by the tool pin (in N-m), μ = Co-efficient of friction for tool and work piece (typically 0.5), F = AL (N), $r_{i\,=}$ Radius of the tool shoulder (m), r_o = Tool pin profile size (m), h = Height of the tool pin (m), T = Total torque (nm), η = Efficiency of welded joints (typically about 0.9), N = TRS (in rpm), f = WS (mm/min), Q_{in} = AHI (in kJ/mm).

The heat generation during the FSW process of AMMHCs across seventeen welding conditions (Figure 1) is initially computed utilizing equation (3), with the results tabulated in table 2. Subsequently, the impact of this heat on growth of grain, transformation of phase within the microstructure, as well as UTS and WNH in the welded zone is thoroughly examined. For PWHT, three distinct FSW AMMHC samples are earmarked, representing conditions of LHI, HHI, and OHI, based on an extensive literature review.

From table 2, trial 4, exhibiting an AHI of 28.55 kJ/mm, is identified as representing LHI conditions, characterized by a TRS of 1000 rpm, WS of 50 mm/min, and AL of 4 kN. Similarly, trial no. 14, with a heating input of 114.23 kJ/mm, is designated as HHI conditions, featuring TRS of 1000 rpm, WS of 25 mm/min, and AL of 8 kN. The HI for the condition representing optimal process parameters is determined as 57.83 kJ/mm [17, 18], corresponding to TRS of 1030.95 rpm, WS of 38.5 mm/min, and AL of 5.88 kN. These specifications are summarized in table 3 and serve as the basis for subsequent PWHT processes.

PWHT

AA6082 is an aluminum alloy that can be strengthened through precipitation hardening (age hardening). During PWHT, fine precipitates (such as Mg_2Si in AA6082) form and uniformly distribute throughout the matrix. These precipitates hinder dislocation movement, leading to an increase in both UTS and micro hardness. Subsequently, in this study, the original hybrid composite employed is AA6082/3 wt.% ZrO_2/5 wt.% B_4C. After FSW, solution annealing and numerous aging treatments were performed on the FS Joined specimens. The PWHT procedures included solution annealing (solutionizing) at 450 °C for 1 h, quenching in water at approximately 0°C, followed by artificial aging treatments at 120 °C for soaking period of 24 h. The primary goal of this research is to enhance the UTS (to surpass 250 MPa) of AA6082/3 wt.% ZrO_2/5 wt.% B_4C, potentially replacing AA6061 alloys and their composites in ship floor or cargo deck construction. Subsequent analysis in all cases includes evaluation of microstructure, UTS, and micro hardness.

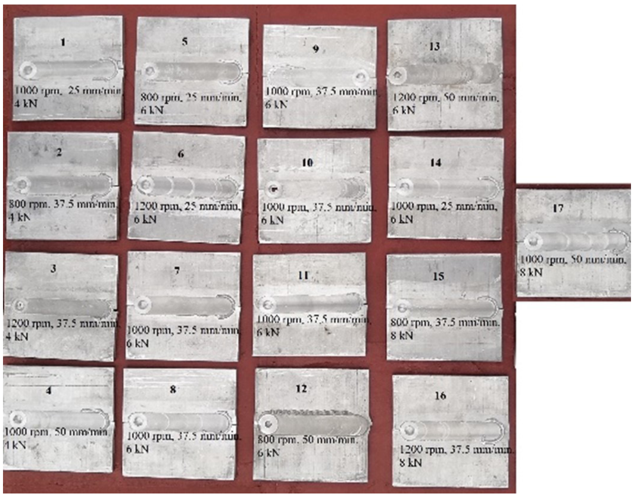

Figure 1: FSW of seventeen samples as per actual design matrix.

Table 2: Heat generated during FSW of AMMHC at various welding conditions.

Number of trial	TRS (rpm)	WS (mm/min)	AL (kN)	UTS (MPa)	WNH (HV)	AHI (kJ/mm)
1	1000	25	4	193	76	57.11
2	800	37.5	4	179	76	30.46
3	1200	37.5	4	210	73	45.69
4	1000	50	4	225	81	28.55
5	800	25	6	181	70	68.54
6	1200	25	6	227	79	102.8
7	1000	37.5	6	251	93	57.11
8	1000	37.5	6	233	95	57.11
9	1000	37.5	6	230	95	57.11
10	1000	37.5	6	239	94	57.11
11	1000	37.5	6	233	95	57.11
12	800	50	6	182	77	34.27
13	1200	50	6	215	76	51.4
14	1000	25	8	198	76	114.23
15	800	37.5	8	186	77	60.92
16	1200	37.5	8	196	75	91.39
17	1000	50	8	189	82	57.11

Table 3: HI conditions considered for PWHT.

Sample No.	HI condition	UTS (MPa)	WNH (HV)	AHI (kJ/mm)
1	LHI	225	81	28.55
2	HHI	198	76	114.23
3	OHI	239.28	94.2	57.83

Metallography and Mechanical Characterization

Metallurgical analysis

An extensive examination of metallurgy on different parts of FSW specimens has been done through the metallurgical microscope at different magnifications. The preparation procedures were as follows: for preparation of FSW welded AMMHC specimens, samples were first cut out size 15 mm × 15 mm × 10 mm then polished with emery papers grit size ranging from 220-1200. After that, the surfaces of the specimens were polished further by means of 6 μm, 3 μm, and 0.5 μm diamond polishing discs. An alumina solution was then applied for the final polishing step to give a bright surface which was later etched with Keller's agent. Such careful preparations allowed for excellent observation conditions at various magnification levels (100X/100 μm, 100X/50 μm, 200X/50 μm) so that BM could be recorded perfectly alongside HAZ, TMAZ as well as WAZ through usage of an optical microscope.

Mechanical tests

ASTM standards E08 M-04 and E10 are followed while assessing how strong FSW joints are based on their mechanical properties. A uniaxial tensile load is applied to characterize elastic-plastic behavior of the material using tensile testing. The tests were carried out with localized strain variations obtained by using an extensometer for measuring the length change of the FSW MMC in control modes of displacement at the speed of 0.1 mm/min. Engineering stress-strain relations were evaluated for each specimen.

The rectangular samples were fabricated for Vickers microhardness test using wire-cut EDM. The dimensions should not exceed 15 mm × 15 mm × 10 mm. They were then subjected to an AL of 500 g for a hold time of 10 s along the centerlines perpendicular to the welding direction on their cross sections: with a 1 mm spacing between the adjacent measuring locations in the weld fusion zone. The indentations made by the indenter measuring 1/16 inch in diameter were measured in various places on the sample's surface to define its sphericity. Various zones within the welded joints had micro hardness assessments carried out at different sections.

Result and Discussions

Examination of microstructure for FSW AMMHCs before PWHT

Figure 2 shows the results of the macrostructure examination of FSW AMMHC for LHI condition (TRS = 1000 rpm, WS = 50 mm/min, and AL = 4 kN). It depicts the WNZ, TMAZ, HAZ, and BM of untreated FSW AMMHC. It also shows the defect-free weld with a narrow weld nugget zone.

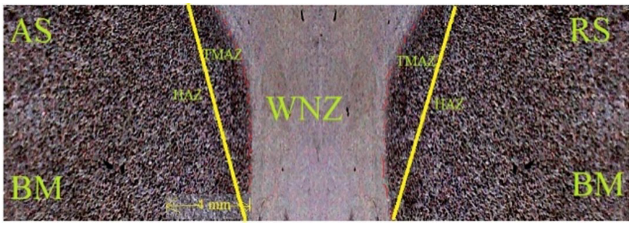

Figure 2: Macrostructure examination of FSW AMMHC for LHI condition before PWHT.

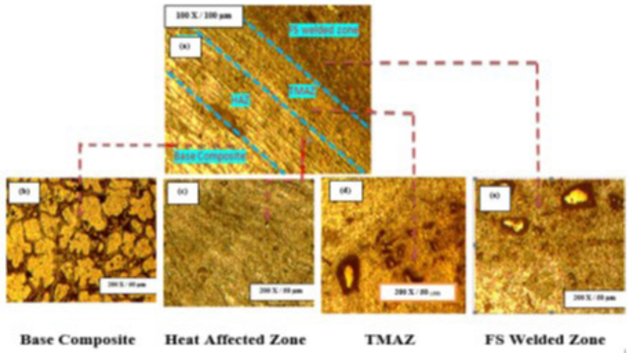

Figure 3: (a) Interfacial zone of FSW AMMHC, **(b)** BM of FSW AMMHC, and **(c-e)** Microstructure examination of FSW AMMHC for LHI condition before PWHT.

Figure 3a shows the interfacial zone of friction stir (FS) welded aluminum matrix metal hybrid composite (AMMHC) under LHI conditions. Distinct zones such as the WNZ, TMAZ, HAZ, and BM are evident. Each zone experiences varying thermal cycles and deformation in the WNZ and TMAZ), resulting in a complex combination of microstructural transformations. The base composite demonstrates substantial material flow in the WNZ and TMAZ, oriented downward, with grains elongated in the same direction. The HAZ, adjacent to the BM, is predominantly impacted by heat and stress due to friction generated by the stirring action. Figure 3b illustrates the base composite with a cast structure of aluminum AMMHC, unaffected by the heat and friction of FS welding. Figure 3c, figure 3d and figure 3e display the results of the microstructural examination of FSW AMMHC for LHI conditions prior to PWHT. Figure 3c focuses on the HAZ, which shows no plastic deformation or grain reinforcement. Figure 3d highlights the TMAZ, where partial recrystallization occurs due to both temperature rise and deformation, with eutectic particle precipitation occurring at the interface of the WNZ and base composite. Figure 3e reveals the WNZ, where plastic deformation caused by the rotating FSW tool leads to a highly recrystallized grain structure. This region also displays dendritic grain fragmentation and the precipitation of eutectic particles as fine particles due to the combined effects of stress and heat.

Figure 4 depicts the macrostructure of FSW AMMHC under HHI conditions confirming the presence of WNZ, TMAZ, HAZ, and BM before the PWHT process. The weld is defect-free and shows a slightly wider WNZ compared to LHI conditions. Similarly, figure 5a presents the interfacial zone of FSW AMMHC for HHI conditions, reaffirming the presence of distinct zones such as WNZ, TMAZ, HAZ, and BM. The base composite exhibits significant flow in the TMAZ and WNZ, with grains elongated in the downward direction, consistent with LHI conditions. As before, the HAZ adjacent to the BM is affected primarily by heat and stress from the stirring action. Figure 5b shows the base composite with a cast aluminum MMC structure that remains unaffected by FS welding. Figure 5c, figure 5d and figure 5e present the microstructural investigation of FSW AMMHC for HHI conditions before PWHT. Figure 5c highlights the HAZ, which, like the LHI condition, does not show plastic deformation or grain reinforcement but displays eutectic particle precipitation at the interface of the WNZ and base composite.

Figure 5d illustrates the TMAZ region, which shows partial recrystallization, experiencing higher temperatures but

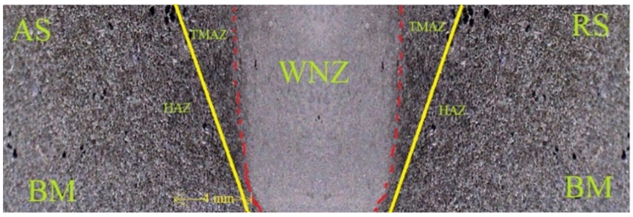

Figure 4: Macrostructure examination of FSW AMMHC for HHI condition before PWHT.

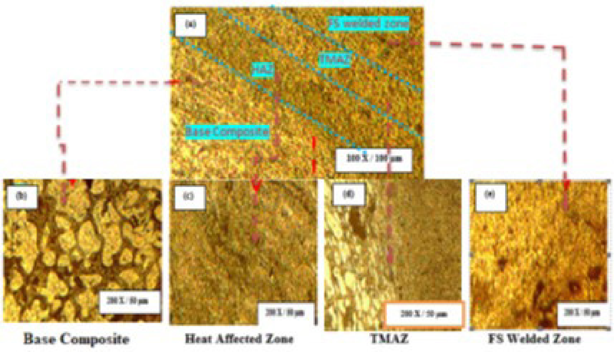

Figure 5: (a) Interfacial zone of FSW MMC, **(b)** BM of FSW AMMHC , and **(c-e)** Microstructure examination of FSW AMMHC for HHI condition before PWHT.

less deformation. It also reveals the precipitation of eutectic particles, along with the connection between the WNZ and the base composite. Figure 5e displays the WNZ region, characterized by reduced plastic deformation due to the rotating FSW tool, yet showing an extremely recrystallized grain structure.

Figure 6 presents the macrostructure examination of FSW AMMHC under HHI conditions corresponding to the OHI conditions. It confirms the presence of WNZ, TMAZ, HAZ, and BM before the PWHT process, with a very narrow weld nugget zone and a defect-free weld.

Figure 7a shows the interfacial zone of FSW AMMHC under OHI conditions before the PWHT process. It reveals the presence of distinct zones such as WNZ, TMAZ, HAZ, and BM. The base composite demonstrates significant material flow in the TMAZ and WNZ, with grains elongated in the downward direction. The HAZ, adjacent to the BM, is primarily affected by heat and stress from the friction generated by the stirring action. Figure 7b illustrates the base composite with a cast structure of aluminum MMC, unaffected by the heat and friction of FS welding. Figure 7c, figure 7d and figure 7e display the results of the microstructural examination of FSW AMMHC under OHI conditions before the PWHT process. Figure 7c focuses on the HAZ region, which shows no plastic deformation or grain reinforcement, but reveals the precipitation of eutectic particles at the interface of the WNZ and base composite. Figure 7d highlights the TMAZ region, where partial recrystallization occurs, along with deformation and a higher temperature rise. Eutectic particle precipitation is also observed, along with the interconnection of the WNZ and base composite.

Figure 7e depicts the WNZ region, which exhibits significant plastic deformation due to the rotating FSW tool, along with a highly recrystallized grain structure. Based on the results obtained for UTS and WNH under the three different HI conditions, the OHI condition achieves a UTS of 239 MPa and a WNH of 94 HV. These values are the highest compared to the other two HI conditions-LHI and HHI conditions.

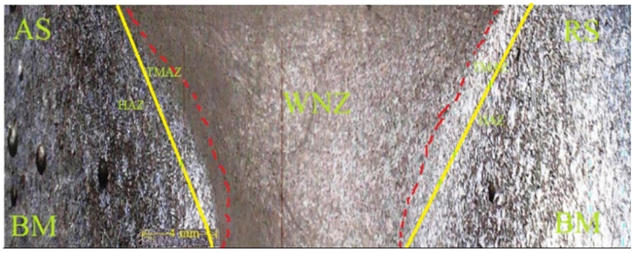

Figure 6: Macrostructure examination of FSW AMMHC for OHI condition before PWHT.

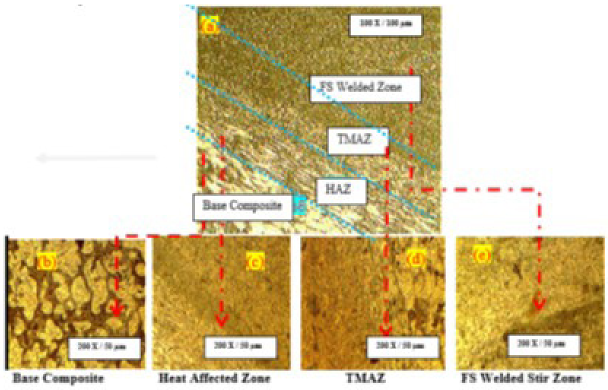

Figure 7: (a) Interfacial zone of FSW MMC, **(b)** BM of FSW MMC, and **(c-e)** Microstructure examination of FSW AMMHC for OHI condition before PWHT.

The microstructure analysis shown in figure 7 demonstrates that the WNH exhibits a fine grain structure with minimal segregation in the matrix. The FSW process transforms the slightly elongated and longer grains found in the BM into a fine, dynamically recrystallized equiaxed grain structure in the WNZ. This grain structure is also more consistently distributed compared to low and HHI conditions. In the WNZ, the fine precipitates become granular after the FSW process, leading to notable variations in mechanical properties across the joint, which could potentially affect joint performance. The grains in the TMAZ are significantly rotated and elongated. Furthermore, it is observed that the TMAZ under both low and HHI conditions is greatly altered by the FSW process, resulting in irregular particulate dislocations. There is no plastic deformation in the HAZ, and the grain structure remains unchanged except for the heating effect. The welding process does not affect the grain size or the precipitate state of the BM. Additionally, the OHI result in well-dispersed grains, minimal particulate dislocations, and good phase dispersion between the BM matrix and particulate reinforcements.

Examination of microstructure for FSW AMMHCs after PWHT at 450 ˚C

After the solution annealing treatment in all three HI conditions (IHI, HHI, and OHI), there are significant changes occurred in the FSW zone of the welds. Huge grains, ranging from numerous hundred microns to a scarce millimeter, were witnessed in the FSW zone, indicating microstructural instability identified as abnormal grain growth. Most of the grain boundaries in the FSW microstructures exhibit great angles (> 15°), classifying the microstructure as recrystallized. Grain growth seems to be a natural significance of solution annealing. Abnormal grain growth in the FSW zone is mainly caused by non-uniform deformation pattern during the FSW process, where the main factors are non-uniform deformation pattern during FSW process. This includes anisotropy of grain boundary energy and mobility reduction of pinning forces resulting from dissolution of particles and thermodynamic driving forces from the distribution of grain sizes. It is very important that we have a good balance of forces that drive the grain to grow abnormally with forces that hinder its movement along the boundaries.

Figure 8a illustrates the interfacial zone of FSW AMMHC under LHI conditions after PWHT. Distinct zones such as WNZ, TMAZ, HAZ, and BM are clearly visible, with the microstructure and properties in these zones largely resembling those described in section 5.1. Figure 8b depicts the base composite, which retains the cast structure of aluminum MMC. Figure 8c shows the HAZ region, which remains free of plastic deformation and grain reinforcement. Figure 8d highlights the TMAZ region, where incomplete recrystallization is observed, along with both temperature rise and deformation. Eutectic particle precipitation is also present, along with the interconnection between the WNZ and the base composite. Figure 8e reveals the WNZ region, which exhibits plastic deformation, and an even more recrystallized grain structure compared to the pre-PWHT grain structure under the same HI conditions. This may explain the improvement in microhardness from 81 HV to 102.3 HV and an increase in UTS from 225 MPa to 242 MPa.

Figure 9a presents the interfacial zone of FSW AMMHC under HHI conditions after PWHT. The WNZ, TMAZ, HAZ, and BM zones are all clearly defined, with the microstructure and properties resembling those discussed in section 5.1. Figure 9b shows the base composite, which retains the cast structure of aluminum MMC. Figure 9c, figure 9d and figure 9e present the results of the microstructural examination of FSW AMMHC under HHI conditions after PWHT. Figure 9c depicts the HAZ region, showing no plastic deformation or grain reinforcement, but eutectic particle precipitation is present, as well as the interconnection between the WNZ and the base composite. Figure 9d illustrates the TMAZ region, which shows partial recrystallization, experiencing higher temperatures but less deformation. Eutectic particle precipitation is also observed, along with the interconnection between the WNZ and the base composite. Figure 9e highlights the WNZ region, showing reduced plastic deformation but a more severely recrystallized grain structure compared to the pre-PWHT condition at the same HI level. This may contribute to an increase in microhardness from 76 HV to 98.8 HV and a slight rise in UTS from 198 MPa to 199 MPa.

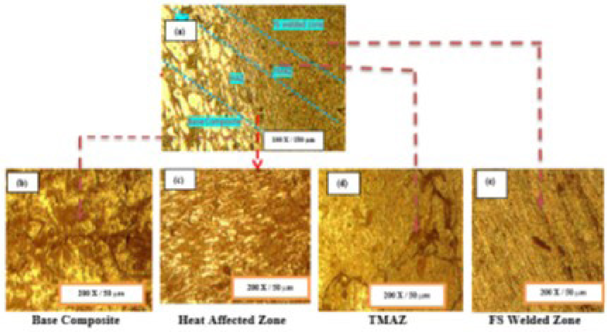

Figure 8: (a) Interfacial zone of FSW MMC, **(b)** BM of FSW MMC, and **(c-e)** Microstructure examination of FSW AMMHC for LHI condition after PWHT at 450 °C.

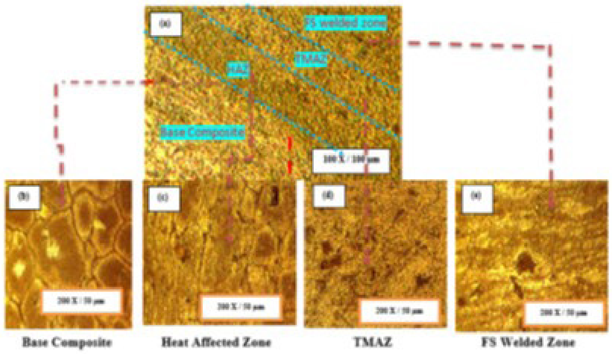

Figure 9: **(a)** Interfacial zone of FSW AMMHC, **(b)** BM of FSW AMMHC, and **(c-e)** Microstructure examination of FSW AMMHC for HHI condition after PWHT at 450 °C.

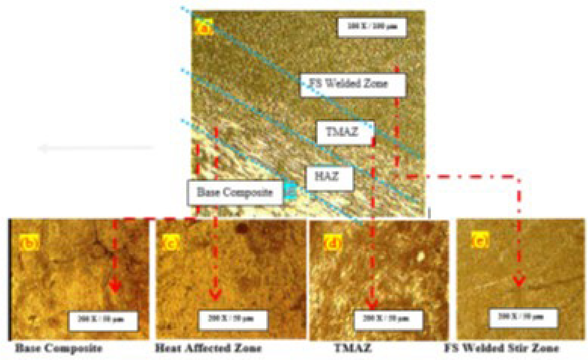

Figure 10: (a) Interfacial zone of FSW AMMHC, **(b)** BM of FSW AMMHC, and **(c-e)** Microstructure examination of FSW AMMHC for OHI condition after PWHT at 450 °C.

Figure 10a illustrates the interfacial zone of FSW AMMHC under optimum FSW process parameter conditions after the PWHT process. It reveals distinct zones, including the WNZ, TMAZ, HAZ, and BM, with all zones exhibiting similar microstructures and properties as described in section 5.1. Figure 10b shows the base composite, retaining its cast aluminum MMC structure. Figure 10c, figure 10d and figure 10e present the results of the microstructure evaluation of FSW AMMHC under optimum FSW process parameter conditions after the PWHT process. Figure 10c focuses on the HAZ region, which does not show any plastic deformation or grain reinforcement. It also reveals the precipitation of eutectic particles and the interconnection between the WNZ and the base composite.

Figure 10d illustrates the TMAZ region, which shows partial recrystallization, experiencing both higher temperatures and deformation. Eutectic particle precipitation is also observed, along with the interconnection between the WNZ and base composite. Figure 10e displays the WNZ region, characterized by severe plastic deformation and an extremely recrystallized grain structure compared to the pre-PWHT grain structure under the same HI conditions. This may explain the increase in microhardness from 94.2 HV to 118 HV and the rise in UTS from 239.28 MPa to 248 MPa.

The microstructure analysis of the FSW process parameter conditions, as shown in figure 10, reveals that the WNH exhibits a fine grain structure, with the matrix in this zone displaying fine grain sizes and low segregation after the PWHT process. The grain structure is also more evenly distributed compared to the low and HHI conditions. Moreover, the optimum FSW process parameter condition demonstrates excellent grain dispersion, fewer particulate dislocations, and superior phase dispersion between the BM matrix and particulate reinforcements after the PWHT process.

In all cases where heat is applied during welding (IHI, HHI, OHI), the temperature of the solution significantly influences the grain stability in the FS alloyed area. Grain expansion typically increases with higher solution temperatures. For all PWHT joints produced in this project, annealing treatment was carried out at a consistent temperature of 450°C for one hour. While the grain sizes in FSW joints do not change significantly after PWHT, there are notable changes in the size and dispersion of the hardening precipitates, depending on the PWHT conditions. These changes are observed in both FS welds and BM, as illustrated in figure 8, figure 9 and figure 10. The microhardness values and tensile properties of the PWHT joints reflect these changes. The static properties of the FSW joints in precipitation-hardening alloys are largely influenced by the distribution of the hardening precipitates rather than by grain size.

The most effective precipitation hardening occurred during the optimal FSW process parameter HI condition, which resulted in significant hardening and toughening compared to the other HI conditions. On the other hand, compared to the LHI condition, the microstructure of FSW joints in the HHI condition exhibited coarse hardening precipitates, with the lowest microhardness and strength values. However, solution annealing improved the microstructure of the weld zone, leading to a more uniform platelet distribution and reduced lag in crystal formation within the welding pool. This, in turn, enhanced both strength and ductility. Consequently, the tensile and hardness test results for these alloys were notably high after high-temperature treatment.

Micro hardness results before and after PWHT

The microhardness results for PWHT at 450 °C are presented in table 4. For FSW advanced metal matrix hybrid composites (AMMHCs), PWHT at 450 °C yields microhardness values of 102.3 HV, 98.8 HV, and 118 HV for LHI, HHI, and optimal FSW process parameter conditions, respectively. These represent improvements of 8.6% (LHI), 4.88% (HHI), and 25.27% (optimal process parameter conditions) compared to the microhardness of FSW AMMHCs without PWHT, which was 94.2 HV under optimal welding process parameters.

Microhardness survey in weldment and UTS before and after PWHT at 450 °C

The microhardness of the stir zone is consistently higher than that of the BM. The base microhardness of the AA6082 alloy and the AMMHC material (AA6082/3%ZrO_2/5%B_4C) is 63 HV and 72.5 HV (optimum value), respectively, representing a 15% improvement compared to the base AA6082 alloy. The microhardness of the stir zone for FSW under optimum parameters is 94 HV, a 27% increase compared to the AMMHC material (AA6082/3%ZrO_2/5%B_4C). This enhancement in microhardness is attributed to the grain refinement in the WNZ, driven by the heat generated during the stirring action of the non-consumable tool. Additionally, solution annealing treatment further refines the grain structure in the WNZ, transforming the coarse grains formed during welding into smaller, more equiaxed, and finer grains, thereby enhancing both UTS and microhardness. As shown in table 4, the maximum microhardness of the stir zone after PWHT for LHI, HHI, and OHI is 102.3 HV, 98.8 HV, and 118 HV, respectively. These represent increases of 8.6%, 4.88%, and 25.27%, respectively, compared to the FSW AMMHC material (AA6082/3%ZrO_2/5%B_4C). These variations are clearly illustrated in figure 11.

Table 5 presents the microhardness survey results before and after PWHT at 450 °C. Microhardness was measured along the weld nugget zone (centreline) at intervals of 2 mm up to 20 mm from either side. This data is plotted in figure 12, which shows microhardness trends before and after PWHT. From the plot, it is evident that microhardness gradually decreases as the distance from the centreline increases. Additionally, the maximum microhardness consistently occurs on the advancing side compared to the retreating side, regardless of different HI conditions and TRSs. The hardness is significantly influenced by the size and distribution of the strengthening precipitates. The microhardness profile across the welded joint between

Table 4: WNH and UTS after PWHT at 450 °C.

Conditions / Mechanical properties	Optimum FSW AA6082/ 3%ZrO_2/ 5%B_4C without PWHT	PWHT of FSW at LHI condition	PWHT of FSW at HHI condition	PWHT of FSW at optimum condition
Micro hardness (HV)	94.2	102.3	98.8	118
% of variation	-	8.6	4.88	25.27

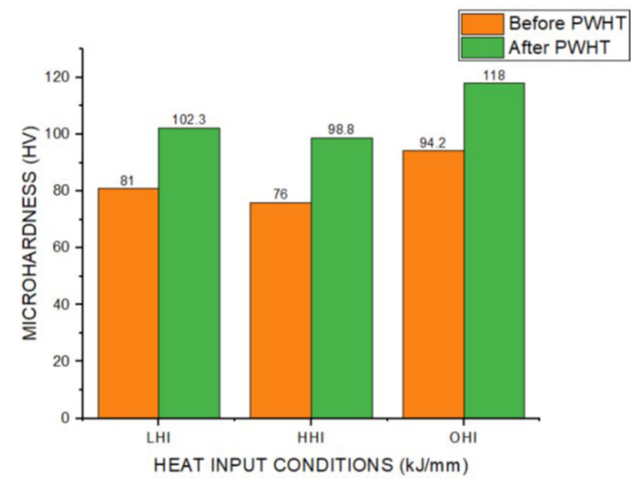

Figure 11: Microhardness for different HI conditions and optimum FSW process parameter HI condition.

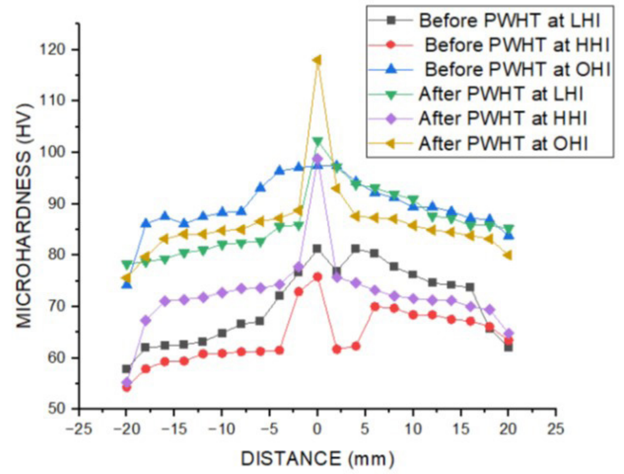

Figure 12: Microhardness survey analysis.

Table 5: Microhardness survey analysis.

Distance from the centerline of WNZ (mm)	Before PWHT			PWHT at 450 °C		
	Low	High	Optimum	Low	High	Optimum
	HV			HV		
-20	57.9	54.3	74.2	78.3	55.2	75.6
-18	62	57.9	86.1	78.7	67.3	79.7
-16	62.3	59.3	87.5	79.3	71.1	83.2
-14	62.6	59.4	86.1	80.5	71.4	84.1
-12	63.2	60.8	87.5	81	71.8	84.1
-10	64.8	60.9	88.3	82.1	72.7	84.8
-8	66.6	61.2	88.5	82.4	73.5	85
-6	67.1	61.3	93.1	82.7	73.6	86.6
-4	72	61.5	96.4	85.6	74.3	87.2
-2	76.6	72.9	97	85.9	77.7	88.7
0	81.2	75.8	97.4	102.3	98.8	118
2	76.9	61.7	97.4	97.2	75.7	93
4	81.2	62.3	94.3	93.8	74.6	87.6
6	80.4	70	92.2	93.1	73.2	87.3
8	77.7	69.7	91.2	91.9	72.1	87.1
10	76.2	68.4	89.4	90.9	71.6	85.8
12	74.6	68.4	89.4	87.6	71.3	84.9
14	74.2	67.5	88.5	87.2	71.2	84.5
16	73.7	67.2	87.2	85.8	70	83.8
18	65.7	66.1	86.9	85.8	69.4	83.2
20	62	63.4	83.8	85.2	64.8	80

AMMHC plates reveals that the regions near the weld are generally softer than the BM and weld nugget zone. This softening is attributed to the dissolution of hardening particles into larger precipitates, which are then overheated beyond their peak aging during welding. However, the finer grain size contributes to some recovery of hardness.

The maximum microhardness values on the advancing side for low, HHI, and optimum FSW conditions are found to be 97.2 HV, 75.7 HV, and 93 HV, respectively. The minimum microhardness values for the same conditions on the advancing side are 85.2 HV, 64.8 HV, and 80 HV, respectively. On the retreating side, the maximum microhardness values for low, HHI, and optimum FSW conditions are 85.9 HV, 77.7 HV, and 88.7 HV, respectively, while the minimum values are 78.3 HV, 55.2 HV, and 75.6 HV, respectively. These variations in microhardness are due to changes in grain size in the welded zone during the FSW process, as microhardness is directly related to grain size. The grain sizes in AMMHCs vary depending on the HI and PWHT conditions.

UTS results before and after PWHT

The UTS results for PWHT at temperatures of 450°C are detailed in table 6 [19-23]. For FSW AMMHCs, PWHT at 450 °C results in UTS values for FSW AMMHCs of 242 MPa, 199 MPa, and 248 MPa respectively for LHI, HHI conditions, and OHI conditions. This demonstrates a 1.14% improvement (LHI condition) and 3.64% improvement (FSW at optimal process parameter conditions) in UTS compared to FSW AMMHCs (239.28 MPa) under optimal welding process parameter conditions without PWHT.

Alloying elements are segregated during the FS welding process, leading to areas of weakness. This solution annealing helped in redistributing these elements more evenly throughout the material, eliminating segregation and resulting in more consistent mechanical properties. Recovery and recrystallization processes during PWHT helped in reducing dislocation density and forming new strain-free grains, which enhanced UTS of this AMMHCs.

It is confirmed from table 6. It is also evident from figure 13 that UTS slightly increases for LHI, HHI conditions, and optimum FSW process parameter conditions. UTS attained after PWHT for LHI, HHI conditions, and optimum FSW process parameter conditions are 242 MPa, 199 MPa, and 248 MPa respectively. There is an increase of 1.14 %, 5.73%, -16.84% and 3.64% respectively UTS as compared to corresponding FSW AMMHC sample before PWHT process. Attained UTS after PWHT at 450 °C for LHI, HHI conditions, and optimum FSW process parameter conditions are 32.24%, 8.19% and 35.52% higher than UTS (183 MPa) obtained for research work during previous studies.

Conclusions

This current examination accords with the studies of solu-

Table 6: UTS before and after PWHT at 450 °C.

Conditions / Mechanical properties	Optimum FSW AA6082/ 3%ZrO_2/ 5%B_4C without PWHT	PWHT of FSW welded at LHI condition	PWHT of FSW welded at HHI condition	PWHT of FSW at optimum condition
UTS (MPa)	239.28	242	199	248
% of variation	-	1.14	-16.84	3.64

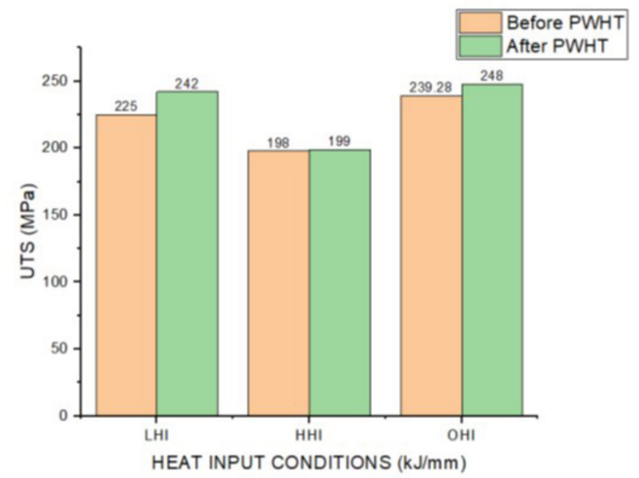

Figure 13: Ultimate tensile strength for various HI conditions and optimum FSW process parameter HI condition.

tion annealing on FSW samples with LHI, HHI conditions, and OHI condition and their influence on the microstructure, WNH, and UTS of FSW joints.

Solution annealing treatment enhances the UTS and WNH of FSW AMMHCs by promoting precipitation hardening, relieving residual stresses, refining the microstructure, reducing weld defects, enhancing solid solution strengthening, modifying grain structure, eliminating segregation, and facilitating recovery and recrystallization processes. These microstructural and stress-related changes collectively contribute to the improved mechanical properties observed after PWHT.

After solution annealing of the FSW joints at 450 °C, abnormal grain growth occurs within the FSW zone. It is observed that the maximum microhardness is consistently found on the advancing side compared to the retreating side, regardless of the HI conditions and different TRSs.

After PWHT at 450 °C, there is an increase in microhardness of 8.6% for LHI condition, 4.88% for HHI condition, and 25.27% for OHI, compared to FSW AMMHCs. Additionally, UTS shows a slight increase for LHI, HHI and OHI conditions.

Specifically, after PWHT at 450 °C, UTS improves by 1.14% for LHI condition, decreases by 16.84% for HHI condition, and increases by 3.64% for OHI condition, compared to FSW AMMHCs.

After PWHT at 450 °C, the FSW AMMHC sample treated under OHI exhibits the highest microhardness of 118 HV and an improved UTS of 248 MPa.

The solution annealing treatment, followed by an artificial aging cycle (450 °C for 60 min and 120 °C for 24 h), significantly enhances the UTS and WNH of FSW AMMHCs.

Acknowledgments

None.

Conflict of Interest

None.

References

1. Pabitra M, Rahul KN, Ranit K, Pritam P, Bhogendro RK, et al. 2021. Effect of post processing heat treatment on friction stir welded/processed aluminum-based alloys and composites. *J Manuf Sc Technol* 35: 96-105. https://doi.org/10.1016/j.cirpj.2021.05.014
2. Mohammad MM, Hamed JA, Roohollah J. 2017. Effect of pre and post welding heat treatment in SiC-fortified dissimilar AA6061-AA2024 FSW butt joint. *J Manuf Process* 30: 97-105. https://doi.org/10.1016/j.jmapro.2017.08.014
3. Feng AH, Xiao BL, Ma ZY. 2008. Effect of microstructural evolution on mechanical properties of friction stir welded AA2009/SiCp composite. *Compos Sci Technol* 68: 2141-2148. https://doi.org/10.1016/j.compscitech.2008.03.010
4. Gupta AK, Lloyd DJ, Court SA. 2001. Precipitation hardening processes in an Al–0.4%Mg–1.3%Si–0.25% Fe aluminum alloy. *Mater Sci Eng* 301: 140-146. https://doi.org/10.1016/S0921-5093(00)01814-1
5. Wang X, Poole WJ, Esmaeili S, Lloyd DJ, Embury JD. 2003. Precipitation strengthening of the aluminum alloy AA6111. *Metal Mater Trans* 34A: 2913-2924. https://doi.org/10.1007/s11661-003-0191-0
6. Bahman M, Mostafa M. 2011. Tensile properties of AA6061 in different designated precipitation hardening and cold working. *Procedia En* 10: 136-140. https://doi.org/10.1016/j.proeng.2011.04.025
7. Ahmad R, Asmael MBA. 2015. Effect of aging time on microstructure and mechanical properties of AA6061 friction stir welding joints. *Int J Automot Mech Eng* 11: 2364-2372. http://dx.doi.org/10.15282/ijame.11.2015.17.0198
8. Jitlada B, Sookkaew K, Kanokwan U, Jirapan D, Chatdanai B, et al. 2015. Post-Weld heat treatment effects on hardness and impact strength of aluminum alloy 6061 friction stir butt weld. *Mater Trans* 56(7): 1072-1076. https://doi.org/10.2320/matertrans.M2015074
9. Yousefpour HN, Omidvar H, Farahmand M. 2016. Investigating the effects of traveling speeds and post-weld heat treatment on mechanical properties of nano-Al_2O_3-fortified AA6061-T6 friction stir welds. *J Mater Design Appl* 232(10): 1-13. https://doi.org/10.1177/1464420716650913
10. Hossein KP, Hamid RJ, Moslem P. 2018. Effect of precipitation hardening heat treatment on mechanical and microstructure features of dissimilar friction stir welded AA2024-T6 and AA6061-T6 alloys. *J Manuf Process* 31: 214-220. https://doi.org/10.1016/j.jmapro.2017.11.019
11. Amir HB, Armin R, Nor FMS, Zainuddin S, Mohd ZO. 2019. Effect of post-weld heat treatment on mechanical behaviour and dislocation density of FSWed Al 6061. *Mater Sci Eng* 754: 728-734. https://doi.org/10.1016/j.msea.2019.03.017

12. Bakkiyaraj M, Palanisamy P, Nagarajan PK, Balasubramanian V. 2020. Effect of post-weld heat treatment on tensile strength and microstructure characteristics in dissimilar friction welded (AA6061–AA7075-T6) joints. *Mater Res Exp* 6(12): 1-22. https://doi.org/10.1088/2053-1591/ab637b
13. Monoj B, Anil B. 2020. Processing and precipitation strengthening of 6xxx series aluminium alloys: a review. *Int J Mater Sci* 1(1): 40-48. https://doi.org/10.22271/27078221.2020.v1.i1a.10
14. Srikantha C, Vaira VR, Padmanaban R. 2021. Investigations on the effect of cyclic heat treatment on the mechanical properties of friction stir welded aluminum alloys (AA5052 & AA6061). *Russ J Non-Ferr Metals* 62(6): 692-707. https://doi.org/10.3103/S1067821221060079
15. Hamilton C, Dymek S, Sommers A. 2008. A thermal model of friction stir welding in aluminum alloys. *Int J Mach Tools Manuf* 48: 1120-1130. https://doi.org/10.1016/j.ijmachtools.2008.02.001
16. Lombard H, Hattingh G, Steuwer A, James AN. 2008. Optimizing FSW process parameters to minimize defects and maximize fatigue life in 5083-H321 aluminium alloy. *Eng Fract Mech* 75(3): 341-354. https://doi.org/10.1016/j.ijmachtools.2008.02.001
17. Umar Mohamed J, Palaniappan PLK, Maran P, Pandiyarajan R. 2020. Investigation and optimization of friction stir welding process parameters of stir cast AA6082/ ZrO_2/B_4C composites. *Mater Sci Poland* 38(4): 715-730. https://doi.org/10.2478/msp-2020-0082
18. Umar Mohamed J, Palaniappan PLK, Maran P, Pandiyarajan R. 2021. Influences of ZrO_2 and B_4C reinforcement on metallurgical, mechanical, and tribological properties of AA6082 hybrid composite materials. *J Ceram Process Res* 22(3): 306-316. https://doi.org/10.36410/jcpr.2021.22.3.306
19. Sivaraj P, Kanagarajan D, Balasubramanian V. 2014. Effect of post weld heat treatment on tensile properties and microstructure characteristics of friction stir welded armour grade AA7075-T651 aluminium alloy. *Def Technol* 10: 1-8. https://doi.org/10.1016/j.dt.2014.01.004
20. Umar Mohamed J, Palaniappan PLK, Maran P. 2022. Influence of post weld heat treatment on the tensile and microhardness characteristics of friction stir welded joints of AA6082/ZrO_2/B_4C composites. *Mater Today Proc* 56: 902-909. https://doi.org/10.1016/j.matpr.2022.02.535
21. Liu HJ, Chen YC, Feng, JC. 2006. Effect of heat treatment on tensile properties of friction stir welded joints of 2219-T6 aluminium alloy. *Mater Sci Technol* 22(2): 237-241. https://doi.org/10.1179/026708306X81513
22. Oztoprak N, Yeni CE, Binnur Goren Kiral BG. 2018. Effects of post-weld heat treatment on the microstructural evolution and mechanical properties of dissimilar friction stir welded AA6061+SiCp/AA6061-O joint. *Lat Am J Solids Struct* 15(8): 1-17. https://doi.org/10.1590/1679-78254553
23. Pandiyarajan R, Prabakaran MP. 2020. Characterization of AA6061-ZrO_2-C friction stir welded composite joints. *J Ceram Process Res* 21(6): 690-698. https://doi.org/10.36410/jcpr.2020.21.6.690